Korean J. Chem. Eng., 38(5), 1052-1058 (2021)
DOI: 10.1007/s11814-021-0772-x

pISSN: 0256-1115
eISSN: 1975-7220

Colloidal synthesis of monodisperse ultrathin $LiFePO_4$ nanosheets for Li-ion battery cathodes

Hyun Hee Oh and Jin Joo†

Department of Applied Chemistry, Kyungpook National University, Daegu 41566, Korea
(*Received 3 February 2021 • Revised 15 February 2021 • Accepted 23 February 2021*)

Abstract—Lithium-ion conductivity is one of the critical factors in improving the rate capability of $LiFePO_4$ in lithium-ion batteries. The one-dimensional diffusion pathway of lithium ions slows the charging/discharging rates in the olivine structure of $LiFePO_4$. Herein, ultrathin $LiFePO_4$ nanosheets were synthesized using surface-passivating ligands to address the rate capability issue. The thickness direction of the nanosheets is the [010] direction in which the lithium ions are inserted or extracted during cycling. The structural and morphological characterizations were performed via transmission electron microscopy and X-ray diffraction. A thickness of 7.5 nm was obtained from the atomic force microscopy height profiles, which is in the scale of twelve unit cells of $LiFePO_4$. Electrochemical performance test results revealed that the Li-ion batteries had superior rate capability during the charging/discharging process.

Keywords: Lithium-ion Batteries, $LiFePO_4$, Olivine Structure, Nanosheets, Electrochemical Performance

INTRODUCTION

The recent expansion of markets for electric vehicles and portable electronics has drawn a great deal of attention to lithium-ion batteries (LIBs). In spite of the substantial improvement in the electrochemical performance of LIBs, there is still a growing demand for a larger reversible capacity, greater rate capability, and longer cycle life. Cathode materials are the main component that limits the progress of LIB technologies, and extensive effort has been made for the development of cathode materials for better electrochemical performance of LIBs [1,2]. Currently, several types of cathode materials are successfully commercialized in the industry. Among them, $LiFePO_4$ has received great attention for its environmental compatibility, cheap raw materials cost, high thermal and chemical stability, and relatively large theoretical capacity (~170 mAh g^{-1}). However, its poor Li-ion conductivity needs to be addressed to improve the rate capability of $LiFePO_4$.

$LiFePO_4$ adopts an olivine crystal structure composed of LiO_6, FeO_6 octahedra, and PO_4 tetrahedra. Its high structural stability stems from the strong P-O bonds, which suppresses the O_2 gas formation at a highly charged state by an Fe-O-X inductive effect [3-5]. According to several studies using computational calculations, Li ions preferably transport throughout the [010] direction; however, the diffusion coefficient along this pathway is as low as ~10^{-14}-10^{-16} cm^2 s^{-1} [6-8], which slows the charge/discharge process. In addition, the presence of intrinsic point defects that are distributed along the [010] channel impedes the Li-ion diffusion during charge/discharge process [9]. One of the strategies to enhance the rate capability of $LiFePO_4$, which is associated with a one-dimensional (1D) slow diffusion of the Li ion through the [010] direction, is to reduce crystal size to a nanometer scale [9-12]. $LiFePO_4$ particles with a short length along the [010] direction enable a large capacity at a high charge/discharge rate. In designing an ideal shape of the $LiFePO_4$ particles, the volumetric energy density is another important factor to consider. Even though spherical nanoparticles have a short [010] channel for Li-ion diffusion, the high surface area of the nanoparticles causes parasitic reactions at the electrode/electrolyte interface [13-15]. Therefore, thin sheet-shaped $LiFePO_4$ particles are desirable to realize a better rate capability of LIBs that are fabricated with the $LiFePO_4$ cathode material.

Several methods have been developed to achieve two-dimensional (2D) nanoplate-shaped $LiFePO_4$ particles, including solvothermal reaction [16], exfoliation [17,18], and colloidal synthesis [19]. The colloidal synthesis of nanoparticles via surface-passivating ligands was first reported in the preparation of monodisperse cadmium chalcogenide quantum dots (QDs) [20]. This method employs ligands that can strongly bind on precursor ions. The nuclei start to form at ~300 °C, which is followed by the growth of the nanoparticles. During the nucleation and growth period, the surface of the particles is dynamically passivated with coordinating ligands, thereby controlling the growth rate in the colloidal state. The binding ability of the ligands to the ions on the surface of the nanoparticles varies depending on the crystal facets and the functionality of the ligands [21]. Using such difference of binding ability between the ligands and the surface ions of the nanoparticles with respect to the crystal facets, 1D nanorods [22], 2D nanoribbon-shaped [23] and 2D nanosheets [24] of cadmium chalcogenides nanoparticles can be synthesized. George et al. successfully introduced the colloidal synthesis for the preparation of $LiFePO_4$ nanoplates with a thickness of ~15 nm [19]. Unfortunately, the characterization method for the estimation of the nanoplate's thickness was not provided in the literature. This study reports monodisperse ultrathin $LiFePO_4$ nanosheets that are prepared using the colloidal synthesis method. Lithium stearate and $FeCl_3$-tri-*n*-octylphosphine (TOP) are used as

†To whom correspondence should be addressed.
E-mail: joojin@knu.ac.kr

Li and Fe precursors, which exhibit high solubility in a ligand mixture composed of oleic acid (OA), oleylamine (OAm), and TOP. The solution of the precursor mixture reacts at an elevated temperature, thereby producing monodisperse $LiFePO_4$ nanosheets with a thickness of ~7.5 nm. This corresponds to the size of twelve unit cells in the [010] direction of the olivine structure of $LiFePO_4$.

EXPERIMENTAL METHODS

1. Materials

$FeCl_3$ (98%, Alfa Aesar), TOP (90%, Fisher Science), lithium stearate (TCI, 90%), diammonium phosphate ($(NH_4)_2HPO_4$, 98%, Aldrich), sucrose (99.5%, Aldrich), and bulk $LiFePO_4$ (>97%, Aldrich) were used as received. OAm (90%, Acros Organics) and OA (90%, Aldrich) were purified by vacuum distillation before use.

2. Synthesis of $LiFePO_4$ Nanosheets

All reactions were performed in an argon atmosphere using standard Schlenk techniques. Ultrathin $LiFePO_4$ nanosheets were synthesized using the colloidal synthesis method. In a typical procedure, 1 mmol of lithium stearate was added in 4 mL of OA with vigorous stirring at 150 °C, followed by the addition of 0.6 mmol of $FeCl_3$ in 6 mL of TOP at room temperature. Concurrently, 1 mmol of $(NH_4)_2HPO_4$ was added in 10 mL of OAm, and the resulting mixture was heated to 275 °C at a heating rate of 5 °C/min under argon atmosphere and maintained at the same temperature for 1 h. The solution containing the lithium and iron precursor was injected into the previously prepared $(NH_4)_2HPO_4$ solution under vigorous stirring. The resulting dark brown solution gradually turned turbid white. After 1 h, the reaction mixture cooled to room temperature by removing the heating mantle. An excess of ethanol was then added, resulting in the precipitation of $LiFePO_4$ nanosheets. The precipitate was isolated by centrifugation, and the purification step of $LiFePO_4$ nanosheets was repeated several times. The produced nanosheets were dispersed in nonpolar organic solvents, such as chloroform and hexane. The $LiFePO_4$ nanosheets were approximately 300-nm sized ellipsoidal particle shape with a thickness of 7.5 nm. Fig. 1 shows the schematic representation of the typical experiment procedure.

3. Characterization

The crystal structure of $LiFePO_4$ was confirmed by X-ray diffraction (XRD, Rigaku D/Max-2500) with a Cu Kα radiation source. Transmission electron microscopy (TEM) and Z-mapping images were obtained with Titan G2 80-200 with ChemiSTEM Technology at 200 kV. The samples for TEM were prepared by dropping dilute solutions of $LiFePO_4$ onto carbon-coated copper grids and evaporating the solvent. An atomic force microscope (AFM, Park Systems XE7) was used to measure the thickness of $LiFePO_4$ using the diluted $LiFePO_4$ solutions to dribble onto the mica and evaporate the solvent. Thermogravimetric analysis (TGA) and differential thermal analysis (DSC) were performed with a TA Instruments SDT Q600 setup at a heating rate of 10 °C/min under an N_2 atmosphere.

4. Electrochemical Measurements

To improve the electronic conductivity, the $LiFePO_4$ nanosheets were overcoated with carbon on the surface. The as-synthesized $LiFePO_4$ nanosheets were dried in a vacuum oven at 60 °C for 3 h. The dried sample was mixed with 10 wt% sucrose as a carbon source and was then carbonized using a tubular furnace at 550 °C for 5 h under an Ar-H_2 (95 : 5) atmosphere with a heating rate of 3 °C/min.

The carbon-coated $LiFePO_4$ nanosheets were used as active materials of the cathode. To prepare the cathode electrode, 94 wt% $LiFePO_4$ (active material), 3 wt% Denka black (conductive material), and 3 wt% of polyvinylidene difluoride (PVDF) (binder) were dispersed in the *N*-methyl-2-pyrrolidinone (NMP). The resulting slurry was coated onto the aluminum foil using the doctor-blade method. The electrode was dried in a vacuum oven at 70 °C for 12 h to remove the remaining solvent, followed by roll pressing. A coin-type half cell (CR2032) was assembled in an argon-filled glove box with the $LiFePO_4$/C nanosheet cathode electrode as the working electrode and Li metal electrode as the reference and counter electrode. The electrolyte was 1.0 M $LiPF_6$ in ethylene carbonate/ethyl methyl carbonate (EC/EMC, 1 : 2 vol%). The capacity and cyclic stability of the cells were characterized on a battery cycler system (WonATech WBCS3000) under a voltage range of 2.0 to 4.5 V (vs. Li/Li^+).

RESULTS AND DISCUSSION

The anisotropic growth of a crystal largely depends on the crystal's surface energy. Wulff's construction explains the crystals' shape in an equilibrium state, where the particles adopt the morphology with the lowest total surface energy. According to the result from simulation techniques for the calculation of surface energy [25], the orthorhombic structure of $LiFePO_4$ tends to have a surface ter-

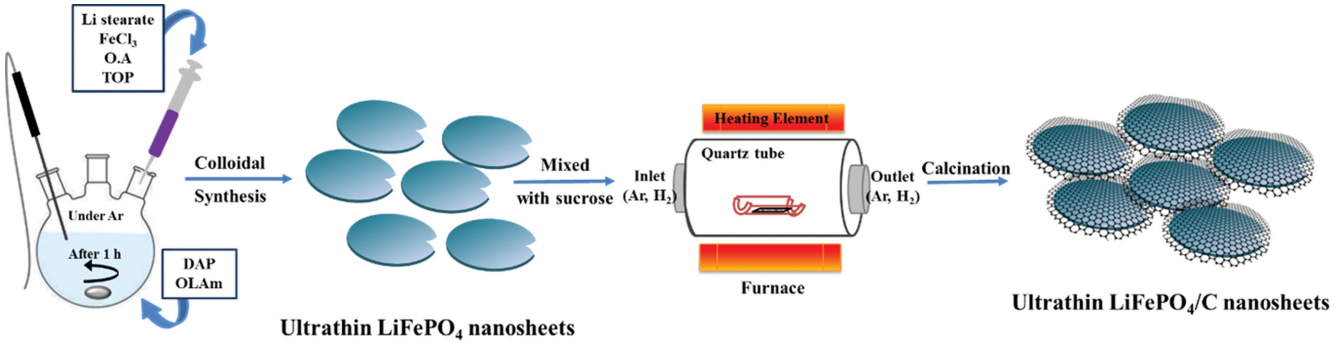

Fig. 1. Schematic illustration of the preparation process for the $LiFePO_4$/C nanosheets.

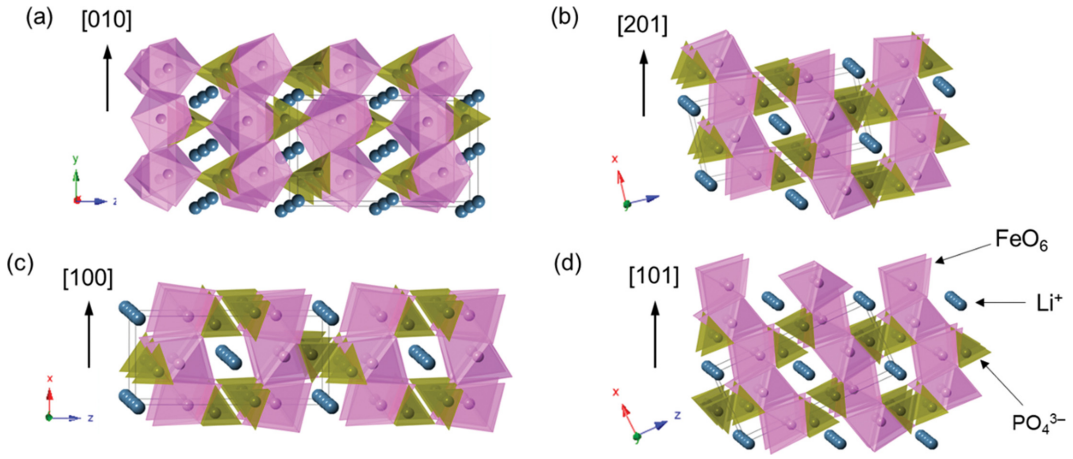

Fig. 2. Crystal structure of $LiFePO_4$ with respect to (a) [010], (b) [201], (c) [100], and (d) [101] directions.

minated mainly by {010}, {201}, {100}, and {101} facets. Among those predominant surface facets, the exposure of {010} plane leads to the lowest surface energy, which is normal to the direction of the Li-ion diffusion during charging/discharging of Li-ion batteries. This lowest surface energy results in an elongated hexagonal prism capped mainly by {010} facets. For the preparation of ultrathin nanoplates of $LiFePO_4$ with the exposure of {010} plane, the differences in the surface energies between the {010} and other planes should be made more pronounced. One promising strategy is the use of surface-passivating ligands. The surface-coordinating ability of organic molecules as surface-passivating ligands differs depending on the functionality of the ligands and the atomic arrangement of the specific surface facets. Thus, a choice of ligands with an appropriate functional group is critical for anisotropic crystal growth. Such a method has been widely used in the shape control of nanoparticles. For example, alkylphosphonic acid strongly passivates the lateral facets in the hexagonal crystal structure of CdSe nanocrystals, producing monodisperse nanorods [22]. In the first report on the synthesis of 2D $LiFePO_4$ nanoplatelets via colloidal synthesis method [19], the thickness of $LiFePO_4$ and $LiFeMnPO_4$ nanoplates was reported to be 15 nm; however, the characterization method and data for the measurement of the nanoplate thickness were not specified. Yan et al. [17] reported a thickness of 3.8-4.6 nm for $LiFePO_4$ nanosheets using the solvothermal method for NH_4FePO_4 with a high-pressure high-temperature (HPHT) supercritical lithiation process. However, the prepared $LiFePO_4$ was not highly monodispersed and the preparation procedure was more complicated than the colloidal method. In the colloidal synthesis of $LiFePO_4$, OAm was employed as a surface-passivating ligands [19]. OAm is popular coordinating ligand used in nanocrystal synthesis, especially for cadmium chalcogenide quantum dots because the primary amine has a high affinity to cadmium cations. It is presumed that the organic ligands with other functionality, such as phosphine or carboxylic acid, would more effectively passivate Fe cations on the $LiFePO_4$ surface than OAm, which have been often studied in the synthesis of iron oxide nanocrystals [26,27]. Islam et al. suggested that the termination of surfaces with Li of 50% deficiency is energetically favorable [25]. In the current synthesis, the organic ligands remove the surface dangling bonds by donating electrons to the exposed Fe atoms on the surface. Therefore, the synthesized $LiFePO_4$ nanocrystals under the ligand-passivating condition should have Fe-terminated surfaces rather than Li-terminated ones. Fig. 2 shows the arrangement of surface atoms on the orthorhombic $LiFePO_4$ crystal along various crystal orientations. Among the four predominant planes, {010} has the highest population density of Fe atoms (2.38 Fe atoms/nm^2), whereas other planes have an atomic density of 0.77-1.57 Fe atoms/nm^2. The passivating ligands form a denser capping layer on {010} surfaces, which prevents the access of the monomers required for crystal growth to the particle surface. As a consequence, the growth of $LiFePO_4$ crystals along the [010] direction is limited and they preferably grow along the direction perpendicular to {010} planes, leading to ultrathin nanoplates.

$(NH_4)_2HPO_4$ was chosen as a phosphate precursor of $LiFePO_4$ because it exhibits a solid state at room temperature and is less harmful [19]. The TGA-DSC in Fig. 3 shows that the $(NH_4)_2HPO_4$ starts to melt and decompose at ~155 °C with a loss of NH_3 (~13%

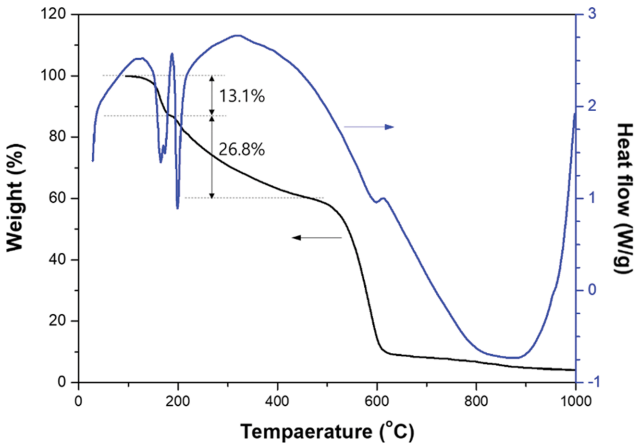

Fig. 3. TGA-DSC curves of $(NH_4)_2HPO_4$ obtained at a heating rate of 10 °C under an N_2 atmosphere. Black and blue solid lines represent the TGA and DSC curves, respectively.

weight loss), which is followed by a second weight loss of NH_3 at ~200 °C (~26% weight loss). Therefore, all syntheses were performed at a high temperature above 250 °C, which is enough to decompose the $(NH_4)_2HPO_4$ precursor, yielding PO_4^{3-} anions. Fe(III) chloride was chosen as the Fe precursor for the mass production of $LiFePO_4$ nanosheets.

The morphology of the synthesized $LiFePO_4$ nanosheets is shown in Fig. 4. A relatively narrow size distribution and a uniform morphology with a length of 250-300 nm and a width of ~100 nm was observed (Fig. 4). All of the nanosheets are translucent, indicating an ultrathin thickness. Interestingly, some of the nanosheets exhibit a spiral growth at a screw dislocation at the center of the nanosheets (Fig. 4(d)). A screw dislocation-driven crystal growth is often observed in inorganic crystals, such as zinc hydroxyl sulfate, α-$Co(OH)_2$, $Ni(OH)_2$, and Au. It was suggested that the spiral growth proceeds when the crystal growth rate at the core of the 2D crys-

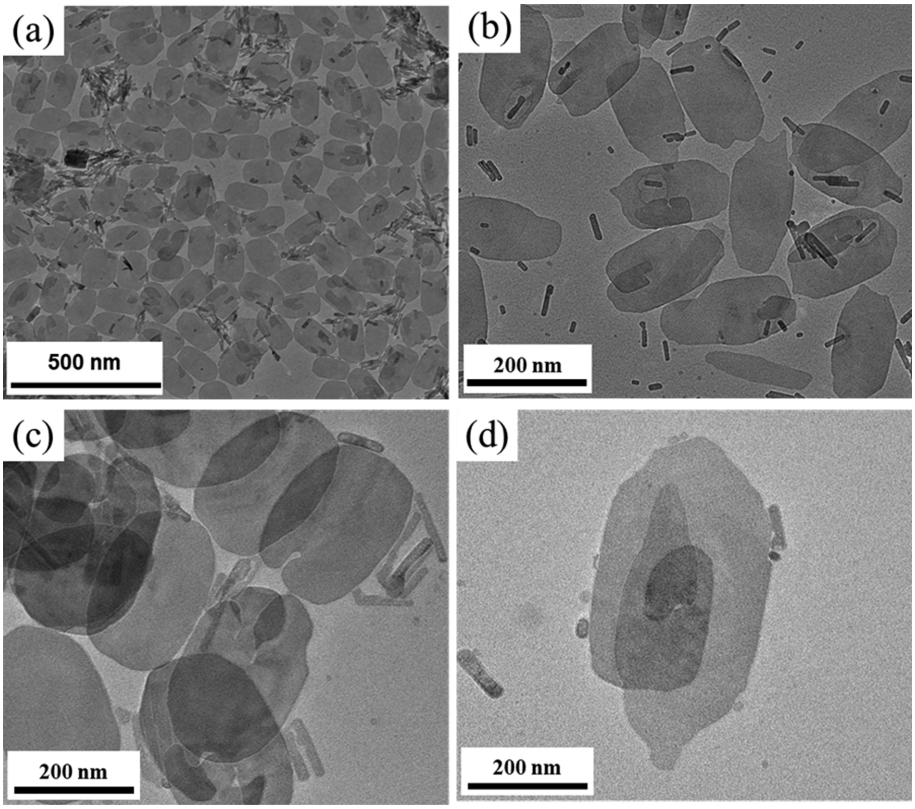

Fig. 4. TEM images of $LiFePO_4$ nanosheets at various magnification.

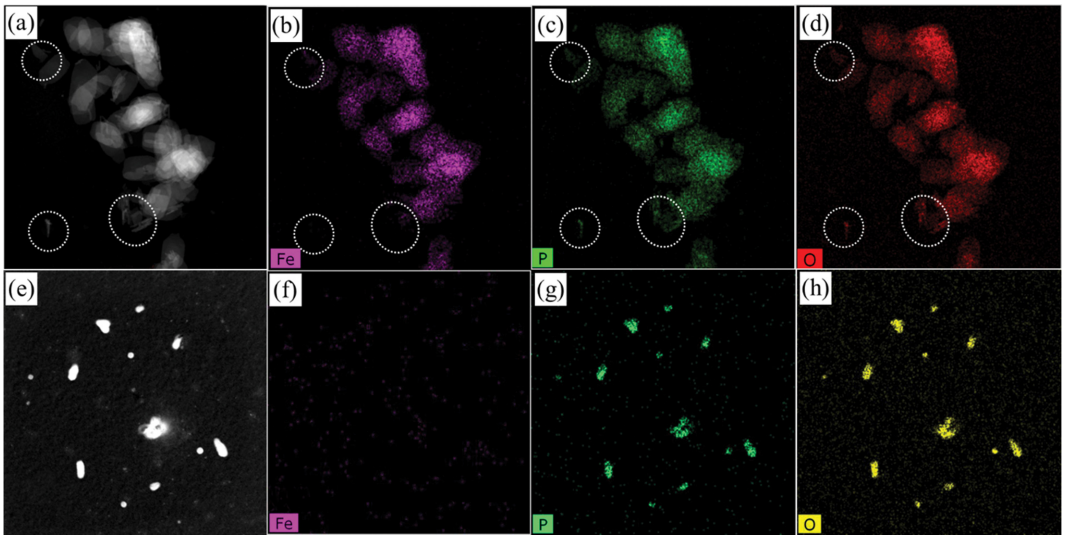

Fig. 5. TEM images and elemental mapping of (a)-(d) $LiFePO_4$ nanosheets and (e)-(h) Li_3PO_4 phase nanoparticles.

tals is similar to the lateral growth velocity under a low supersaturation condition [28,29]. Indeed, the samples that were synthesized for a prolonged growth period tend to have a more spiral shape because most of the required monomers for nanosheet growth are consumed in a longer growth time, achieving a low supersaturation condition. Fig. 5(a)-(d) shows the TEM image and elemental mapping of the $LiFePO_4$ nanosheets. Obviously, all the elements comprising $LiFePO_4$ are evenly distributed over the nanosheets, revealing that all the sheet-shaped particles are $LiFePO_4$ except for lithium. Because the scattered electron beam intensity is proportional to the atomic number, the lithium contained in the sample is hardly visible under the normal elemental imaging technique [30]. In the TEM images (Fig. 4), a small amount of non-sheet shaped particles is observed with the $LiFePO_4$ nanosheets. Likewise, similar non-sheet shaped particles are seen in the elemental mapping image (white dotted circles of Fig. 5(a)-(d)). Interestingly, these non-sheet shaped particles have negligible amount of Fe atoms (Fig. 5(b)). Careful examination was conducted in the TEM grid region with highly distributed those impurity phases (Fig. 5(e)). For the non-sheet shaped particles, phosphorous and oxygen atoms are detected other than the Fe atoms as shown in Fig. 5(f)-(h). From the observation, these impurities are thought to be Li_3PO_4. Li_3PO_4 is one of the materials used to increase the conductivity of the lithium ions in the cathode materials. For instance, Li_3PO_4 was overcoated on the cathode active materials of $LiCoO_2$ [31] and $LiFePO_4$ [32], resulting in greater rate capability and cycle stability.

For the crystallographic characterization of ultrathin $LiFePO_4$ nanosheets, thin film and powder samples were prepared. The thin film sample of the nanosheets was fabricated by drop-casting the colloidal solution of $LiFePO_4$ nanosheets on the XRD sample holder and, subsequently, by slowly evaporating the dispersion solvent. The powder form was prepared by the addition of poor solvent into the $LiFePO_4$ colloidal solution, followed by centrifugation. Fig. 6 shows the XRD patterns obtained from the film and power form of $LiFePO_4$ nanosheets. Most of the peaks correspond well to those of the bulk orthorhombic structure of $LiFePO_4$ except for the diffraction intensity. Unlike the diffraction pattern of the bulk (bars on the bottom of Fig. 6), the powder-type $LiFePO_4$ nanosheets

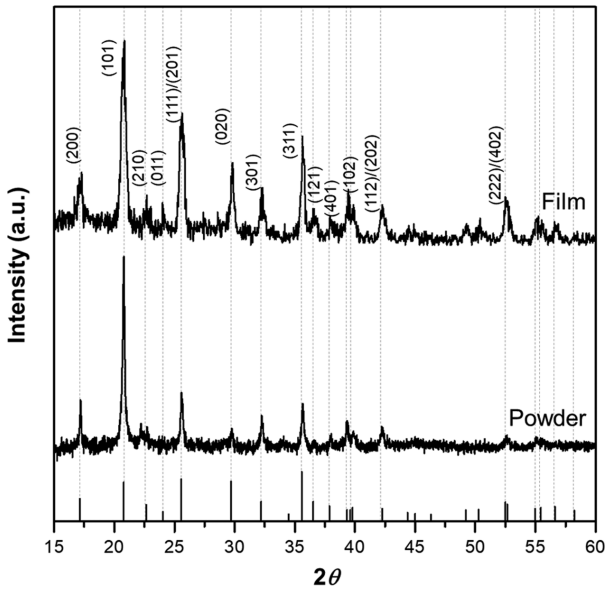

Fig. 6. XRD patterns of (top) film-type and (bottom) powder-type $LiFePO_4$ nanosheets. The bars on the bottom represent the XRD peaks of bulk $LiFePO_4$ (JCPDS file No. 83-2092).

exhibit a smaller intensity from the (020) plane compared to that from the (101) plane. The intensity ratios $I_{(101)}/I_{(020)}$ are 10.5 and 0.97 for the powder form and the bulk $LiFePO_4$ nanosheets, respectively. Accordingly, all other diffraction peaks with the k component in the Miller indices have less intense peaks than the bulk. This means that the crystal size along the [010] direction is much smaller than what it should be when the $LiFePO_4$ has an isotropic crystallite shape, indicating the thin sheet type morphology of our sample. Comparing the intensities of the powder and the film-type nanosheets, the film-type sample shows a larger $I_{(101)}/I_{(020)}$ ratio (10.5 for powder sample and 2.5 for film sample). This is because the slow solvent evaporation of the $LiFePO_4$ colloidal solution induces the arrangement of the nanosheets parallel to the XRD sample holder, under which the diffraction occurs mostly from the crystal plane parallel to the substrate, which is the crystal plane

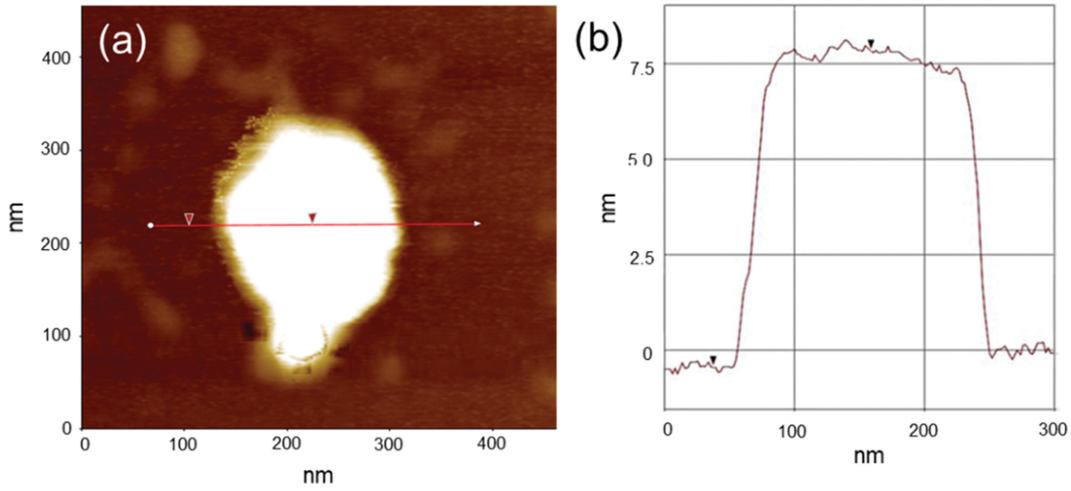

Fig. 7. (a) AFM image of single $LiFePO_4$ nanosheets and (b) the height profile of the corresponding nanosheet represented in Fig. 7(a).

with the k component for our case. Therefore, the pronounced $I_{(101)}/I_{(020)}$ value of the film type sample strongly supports the thin morphology of the synthesized $LiFePO_4$ nanocrystals and the crystallographic orientation in their thickness is confirmed to be along the [010] direction.

AFM topography images are provided in Fig. 7 for the estimation of the nanosheet thickness. The size of the single nanosheet is in good accordance with that from TEM analysis. The single nanosheet with an ellipsoidal symmetry exhibits a size of ~200 nm× 260 nm. The ellipsoidal image viewed from the top and the plateau in the height profile over the whole particle indicates the sheet-shaped particle morphology. The obtained height profile elucidates ~7.5 nm thickness. Considering the lattice parameter of $LiFePO_4$ in the *b*-axis (6 Å), the thickness of the nanosheets is in the twelve-unit cell scale.

The cyclic performance of the $LiFePO_4$ nanosheet electrode and the bulk $LiFePO_4$ (control sample) was compared after carbon coatings, where the lithium metal was used as a counter electrode. Under a 1 C charging/discharging rate, $LiFePO_4$ nanosheets exhibit a superior capacity (132 mAh g^{-1}) compared to the bulk $LiFePO_4$ cathode (107 mAh g^{-1}) after the first cycle as shown in Fig. 8. Moreover, the capacity retention of nanosheet cathode is ~92%, whereas that of the bulk $LiFePO_4$ is ~77% after 100 cycles. The better cyclic stability of the nanosheet cathode compared to that of the bulk is attributed to the fast Li ion diffusion through an ultrathin pathway along the [010] direction of the olivine crystal of $LiFePO_4$ nanosheets. In addition to the advantage of short distance for Li-ion diffusion into $LiFePO_4$ nanosheets, nanoparticles of $LiFePO_4$ (<40 nm) undergo phase transition between $LiFePO_4$ and $FePO_4$ *via* a formation of single solid solution of Li_xFePO_4 ($0 \le x \le 1$) [33,34]. In contrast to the single phase transition, the phase transition of the bulk $LiFePO_4$ occurs between $LiFePO_4$ and $FePO_4$, producing the sharp phase boundaries. The lattice strain at the grain boundaries causes the pulverization of $LiFePO_4$ materials during charging/discharging process. It is believed that ultrathin $LiFePO_4$ effectively suppresses the formation of grain boundaries, contributing to the greater capacity retention than the bulk $LiFePO_4$ [35].

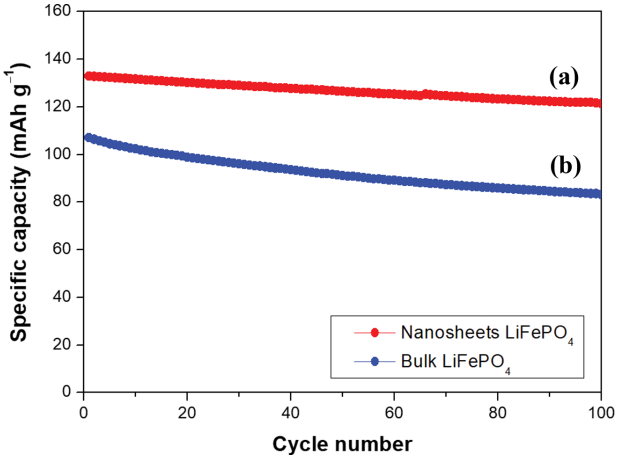

Fig. 8. Cyclic stability of $LiFePO_4$ nanosheets (a) and bulk $LiFePO_4$ (b) cathodes with Li anodes as a counter and reference electrode.

CONCLUSIONS

This study describes the synthesis of ultrathin $LiFePO_4$ nanosheets with a narrow size distribution. Using an optimized combination of surface-passivating ligands, ultrathin nanosheets of olivine-structured $LiFePO_4$ were realized. Structural and morphological characterization confirmed the thickness of ~7.5 nm in the [010] direction of the nanosheets, which enables greater electrochemical performance than the cathode prepared using bulk $LiFePO_4$. $LiFePO_4$ nanosheets delivered a specific capacity of 132 mAh g^{-1}, whereas that of the bulk $LiFePO_4$ cathode was 107 mAh g^{-1} in the first cycle. The nanosheet cathode also provides superior cyclic retention than the bulk $LiFePO_4$ cathode after 100 cycles (92% *vs.* 77%). Further studies to combine graphene with $LiFePO_4$ nanosheets as a cathode are currently underway to maximize the morphological effect during the charging/discharging process.

ACKNOWLEDGEMENTS

This work was supported by the Korea Evaluation Institute of Industrial Technology (KEIT) grant funded by the Ministry of Trade, Industry and Energy, Republic of Korea (Grant No. 20012453).

REFERENCES

1. E. Lim, J. Chun, C. Jo and J. Hwang, *Korean J. Chem. Eng.*, In press (2021).
2. D. Kwak, W.-G. Lim, K. Shin, I. W. Cheong, J. Lee and J. Joo, *Korean J. Chem. Eng.*, **37**, 1258 (2020).
3. A. Yamada, S. C. Chung and K. Hinokuma, *J. Electrochem. Soc.*, **148**, A224 (2001).
4. J. Wang and X. Sun, *Energy Environ. Sci.*, **5**, 5163 (2012).
5. A. Michel, J. B. Goodenough, A. K. Padhi, K. S. Nanjundaswamy and C. Masquelier, US Patent, 6,514,640 (2003).
6. J. Wang and X. Sun, *Energy Environ. Sci.*, **5**, 5163 (2012).
7. P. P. Prosini, M. Lisi, D. Zane and M. Pasquali, *Solid State Ionics*, **148**, 45 (2002).
8. L.-X. Yuan, Z.-H. Wang, W.-X. Zhang, X.-L. Hu, J.-T. Chen, Y.-H. Huang and J. B. Goodenough, *Energy Environ. Sci.*, **4**, 269 (2011).
9. R. Malik, D. Burch, M. Bazant and G. Ceder, *Nano Lett.*, **10**, 4123 (2010).
10. C. Yang, D. J. Lee, H. Kim, K. Kim, J. Joo, W. B. Kim, Y. B. Song, Y. S. Jung and J. Park, *RSC Adv.*, **9**, 13714 (2019).
11. K. Saravanan, P. Balaya, M. V. Reddy, B. V. R. Chowdari and J. J. Vittal, *Energy Environ. Sci.*, **3**, 457 (2010).
12. C. Delacourt, P. Poizot, S. Levasseur and C. Masquelier, *Electrochem. Solid-State Lett.*, **9**, A352 (2006).
13. Y. Zhao, L. Peng, B. Liu and G. Yu, *Nano Lett.*, **14**, 2849 (2014).
14. A. Aricò, P. Bruce, B. Scrosati, J.-M. Tarascon and W. van Schalkwijk, *Nat. Mater.*, **4**, 366 (2005).
15. P. G. Bruce, B. Scrosati and J.-M. Tarascon, *Angew. Chem. Int. Ed.*, **47**, 2930 (2008).
16. L. Wang, X. He, W. Sun, J. Wang, Y. Li and S. Fan, *Nano Lett.*, **12**, 5632 (2012).
17. X. Rui, X. Zhao, Z. Lu, H. Tan, D. Sim, H. H. Hng, R. Yazami, T. M. Lim and Q. Yan, *ACS Nano*, **7**, 5637 (2013).

18. Y. Zhao, L. Peng, B. Liu and G. Yu, *Nano Lett.*, **14**, 2849 (2014).
19. A. Paolella, G. Bertoni, S. Marras, E. Dilena, M. Colombo, M. Prato, A. Riedinger, M. Povia, A. Ansaldo, K. Zaghib, L. Manna and C. George, *Nano Lett.*, **14**, 6828 (2014).
20. C. B. Murray, D. J. Norris and M. G. Bawendi, *J. Am. Chem. Soc.*, **115**, 8706 (1993).
21. M. A. Boles, D. Ling, T. Hyeon and D. V. Talapin, *Nat. Mater.*, **15**, 141 (2016).
22. X. Peng, L. Manna, W. Yang, J. Wickham, E. Scher, A. Kadavanich and A. P. Alivisatos, *Nature*, **404**, 59 (2000).
23. J. Joo, J. S. Son, S. G. Kwon, J. H. Yu and T. Hyeon, *J. Am. Chem. Soc.*, **128**, 5632 (2006).
24. F. Gerdes, C. Navío, B. H. Juárez and C. Klinke, *Nano Lett.*, **17**, 4165 (2017).
25. C. A. J. Fisher and M. S. Islam, *J. Mater. Chem.*, **18**, 1209 (2008).
26. T. Hyeon, S. S. Lee, J. Park, Y. Chung and H. B. Na, *J. Am. Chem. Soc.*, **123**, 12798 (2001).
27. J. Park, K. An, Y. Hwang, J.-G. Park, H.-J. Noh, J.-Y. Kim, J.-H. Park, N.-M. Hwang and T. Hyeon, *Nat. Mater.*, **3**, 891 (2004).
28. F. Wang and X. Wang, *Nanoscale*, **6**, 6398 (2014).
29. S. A. Morin, A. Forticaux, M. J. Bierman and S. Jin, *Nano Lett.*, **11**, 4449 (2011).
30. S. Ahmed, M. Bianchini, A. Pokle, M. S. Munde, P. Hartmann, T. Brezesinski, A. Beyer, J. Janek and K. Volz, *Adv. Energy Mater.*, **10**, 2001026 (2020).
31. Y. Jin, N. Li, C. H. Chen and S. Q. Wei, *Electrochem. Solid-State Lett.*, **9**, A273 (2006).
32. S.-X. Zhao, H. Ding, Y.-C. Wang, B.-H. Li and C.-W. Nan, *J. Alloys Compd.*, **566**, 206 (2013).
33. P. Gibot, M. Casas-Cabanas, L. Laffont, S. Levasseur, P. Carlach, S. Hamelet, J.-M. Tarascon and C. Masquelier, *Nat. Mater.*, **7**, 741 (2008).
34. X. Zhang, M. van Hulzen, D. P. Singh, N. H. van Dijk and M. Wagemaker, *Nat. Commun.*, **6**, 8333 (2015).
35. A. Paolella, G. Bertoni, E. Dilena, S. Marras, A. Ansaldo, L. Manna and C. George, *Nano Lett.*, **14**, 1477 (2014).